electronics

MDPI

Article

A Wideband Non-Stationary 3D GBSM for HAP-MIMO Communication Systems at Millimeter-Wave Bands

Wancheng Zhang, Linhao Gu, Kaien Zhang, Yan Zhang *, Saier Wang and Zijie Ji

School of Information and Electronics, Beijing Institute of Technology, Beijing 100081, China; zhangwancheng@bit.edu.cn (W.Z.); 3220210588@bit.edu.cn (L.G.); zhangkaien@bit.edu.cn (K.Z.); wsaier@bit.edu.cn (S.W.); jizijie@bit.edu.cn (Z.J.)

* Correspondence: zhangy@bit.edu.cn

Abstract: High-altitude platforms (HAPs) are considered to be the most important equipment for next-generation wireless communication technologies. In this paper, we investigate the channel characteristics under the configurations of massive multiple-input multiple-output (MIMO) space and large bandwidth at millimeter-wave (mmWave) bands, along with the moving essence of the HAP and ground terminals. A non-stationary three-dimensional (3D) geometry-based stochastic model (GBSM) is proposed for a HAP communication system. We use a cylinder-based geometric modeling method to construct the channel and derive the channel impulse response (CIR). Additionally, the birth–death process of the scatterers is enclosed using the Markov process. Large-scale parameters such as free space loss and rainfall attenuation are also taken into consideration. Due to the relative motion between HAP and ground terminals, the massive MIMO space, and the wide bandwidth in the mmWave band, the channel characteristics of HAP exhibit non-stationarities in time, space, and frequency domains. By deriving the temporal auto-correlation function (ACF), we explore the non-stationarity in the time domain and the impact of various parameters on the correlations across the HAP-MIMO channels. The spatial cross-correlation function (CCF) for massive MIMO scenarios, and the frequency correlation function (FCF) in the mmWave bands are also considered. Moreover, we conduct simulation research using MATLAB. Simulation results show that the theoretical results align well with the simulation results, and this highlights the fact that the constructed 3D GBSM can characterize the non-stationary characteristics of HAP-MIMO channels across the time, space, and frequency domains.

Keywords: geometry-based stochastic models (GBSM); high-altitude platforms (HAP); Markov process; massive multiple-input multiple-output (MIMO); millimeter wave (mmWave); non-stationary

Citation: Zhang, W.; Gu, L.; Zhang, K.; Zhang, Y.; Wang, S.; Ji, Z. A Wideband Non-Stationary 3D GBSM for HAP-MIMO Communication Systems at Millimeter-Wave Bands. *Electronics* **2024**, *13*, 678. https://doi.org/10.3390/electronics13040678

Academic Editor: Dimitra I. Kaklamani

Received: 10 January 2024
Revised: 31 January 2024
Accepted: 2 February 2024
Published: 6 February 2024

1. Introduction

Recently, there has been a growing demand for flexible and agile connection solutions due to the increasing complexity of wireless communication and the proliferation of communication equipment [1–3]. To meet the demands, non-terrestrial networks (NTNs) have been introduced as part of sixth-generation (6G) technologies, enabling communication from urban centers to remote areas [4,5]. The integrated air and terrestrial systems have been widely discussed by industries and academics [6]. Non-terrestrial network refers to networks, or segments of networks, that use an airborne or spaceborne vehicle for transmission, including satellites, high-altitude platform (HAP) stations, unmanned aircraft vehicles (UAVs), and so on [7]. Among them, HAP communication has gained considerable attention among researchers and practitioners. HAP is a crucial component of air-to-ground networks, providing access to many mobile and internet of things (IoT) users, particularly in rural areas with limited ground base station coverage [8,9]. Compared to traditional communication methods, HAP communication systems offer several advantages, including wide coverage, high bandwidth transmission, quick deployment,

and innovative approaches to expand and enhance communication networks [10–13]. To realize high-performance HAP communication, it is crucial to accurately characterize its propagation channel and build accurate models [14].

The HAP communication model consists of two parts: stratospheric base station (SBS) and terrestrial mobile station (TMS), and they are constantly in motion. The SBS is located between 17 km and 22 km above the ground, and the high-altitude environment is very complex. Therefore, in the process of HAP modeling, it is necessary to consider the non-stationary characteristics in the time domain and the impact of large-scale parameters such as free space path loss and rainfall fading on the channel [15]. In [16], an efficient Markov-chain-based channel model was proposed for HAP communication channels. However, it did not take into account the dynamic propagation environment in practice. In order to more accurately simulate the transmission of signals in complex propagation environments, a 3D geometry-based stochastic model (GBSM) based on cylinders was proposed for HAP communication system in [17]. The birth–death process of the scatterers was considered in [18]. However, due to the high elevation angle, the Parsons pdf used was not appropriate. In [19], Markov processes were employed to describe scatterers' dynamic behavior. The non-stationary characteristics in the time domain of HAP channels were studied, and the influence of some parameters on the statistical characteristics of GBSM was simulated in [20,21]. However, they did not consider the impact of large-scale parameters on the channel.

Incorporating multiple-input multiple-output (MIMO) technology into HAP communication can improve spectral efficiency and reduce attenuation by utilizing spatial and multiplexing gains [22,23]. In [24], the author constructed a 2×2 HAP-MIMO channel. The non-stationary characteristics in the HAP-MIMO channel were analyzed in [25]. However, in practical applications, we often need to use massive MIMO to provide high gain and directional beams. When using massive MIMO, there are non-stationary characteristics in the space domain, which have not been considered in previous work.

With the development of 6G technology, it is expected that HAP communication will achieve higher channel capacity and meet the growing data demand, especially in emerging technologies such as autonomous driving and virtual reality [26,27]. There is a clear need for HAP communication systems that can provide higher bandwidths and faster data transfer rates. World Radiocommunication Conference 2019 (WRC-19) adopted the topic of "Promoting People's Access to Broadband Applications Provided through High Altitude Platform Stations" and proposed a new 38 GHz–39.5 GHz frequency band for HAP globally under a fixed business division [28]. Therefore, studying the HAP communication characteristics in the mmWave band is also very important [29]. As the frequency increases to the mmWave band, HAP requires a wider bandwidth. The model proposed in [30] was extended to a wideband channel model. The statistical characteristics of non-stationary wideband HAP-MIMO channel models were analyzed in [31,32]. However, none of the above models have taken into account the non-stationary characteristics of wide bandwidth in the frequency domain.

To address these challenges, we propose a non-stationary 3D wideband GBSM where scatterers are distributed on the surface of a cylinder following Markov birth–death processes. Large-scale parameters, such as free space loss and rainfall fading, are considered to enhance the accuracy of the channel model. Furthermore, to analyze the non-stationary behavior of the channel, we derive the temporal auto-correlation function (ACF), spatial cross-correlation function (CCF), and frequency correlation function (FCF), and conduct simulation verification. We also consider the impact of different channel parameters on temporal ACF.

The contributions of our research can be summarized as follows.

- A wideband non-stationary 3D GBSM for HAP-MIMO communication systems at mmWave bands is established, which consider the impact of large-scale parameters on the channel.

- The dynamic birth–death behavior of scatterers is modeled through Markov processes. Based on the proposed non-stationary 3D GBSM, some important statistical properties, i.e., temporal ACF, spatial CCF, and FCF, are derived and analyzed.
- The impacts of some parameters on ACF are compared, and the non-stationary characteristics in time, space, and frequency domains are investigated thoroughly by simulations.

The remainder of this paper is organized as follows. Section 2 introduces the composition and transmission characteristics of the HAP-MIMO channel model. Section 3 derives the channel statistics, i.e., the ACF, CCF, and FCF formula. The simulation settings and results are shown in Section 4. Conclusions are drawn in Section 5.

2. Channel Model

2.1. Descriptions of 3D GBSM for HAP-MIMO Channel

Typically, geometric modeling methods based on ellipsoids, hemispheres, and cylinders are used [33–35]. However, the ellipsoid model is only suitable for situations where the receiver is higher than the scatterers. The channel model based on hemispheres usually assumes that the elevation and azimuth angles of the propagation path are correlated. These models can only be applied to specific scenarios and are not perfectly applicable to HAP environments. Nevertheless, the model based on cylinders can adapt to open channel environments and is particularly suitable for situations with high transmitting ends. Therefore, we choose the cylinder model for the HAP channel.

This paper considers a downlink channel with n_T transmit antennas and n_R receive antennas in SBS and TMS, respectively. As shown in Figure 1, we propose a 3D GBSM for HAP-MIMO channel and demonstrate its line-of-sight (LoS) and non-line-of-sight (NLoS) paths, which is the foundation for constructing a uniform linear array with any number of antennas. The two connecting lines between HAP and points m as well as n, represent the LoS path. The two lines that reach the midpoint S represent the NLoS path. The height of the cylinder is H, and the radius is R. We assume that there is no scatterer in the SBS, and the SBS moves at a speed of v_a. S_n ($n = 1, 2, \ldots, N$) denotes scatterers located on the surface of the cylinder. Scatterers and the TMS move together at a speed of v_b. δ_T and δ_R denote the distance between two adjacent antenna elements at the TMS and the SBS, respectively, angles ψ_R denotes the elevation angle of the TMS antenna element in the x–y plane, angles θ_T and θ_R describe the antenna orientations. The heights of O_T and O_R are H_T and H_R, respectively, and the projection distance between them on the x–y plane is D. The elevation angle of O_T relative to O_R is β_T ,which is approximately equal to $\arctan(H_T/D)$. For the ease of reference, we summarize the parameters of the proposed model in Table 1.

We assume that both the receiving and transmitting ends utilize uniformly linear arrays for their antenna configurations. Therefore, the channel between the HAP and the TMS can be modeled as

$$H(t;\tau) = \begin{bmatrix} h_{1,1}(t;\tau) & \cdots & h_{1,n_R}(t;\tau) \\ \vdots & \ddots & \vdots \\ h_{n_T,1}(t;\tau) & \cdots & h_{n_T,n_R}(t;\tau) \end{bmatrix}_{n_T * n_R}, \quad (1)$$

where the matrix element $h_{n_T n_R}(t;\tau)$ represents the channel impulse response (CIR) of the subchannel between the n_R-th receive antenna and the n_T-th transmit antenna.

Table 1. Definition of the parameters in the 3D HAP-MIMO model.

Parameter	Meaning
n_T, n_R	The number of transmit antennas and receive antennas, respectively.
H_T, H_R	The height of TMS and SBS, respectively.
δ_T, δ_R	The spacing between two adjacent antenna elements at the TMS and the SBS, respectively.

Table 1. *Cont.*

Parameter	Meaning
v_a, v_b	The velocity of TMS and SBS, respectively.
β_T	The elevation angle of TMS relative to SBS.
H	The height of the cylinder.
R	The radius of the cylinder.
S_n	The position of the nth scatterer.
ψ_R	The elevation angle of the TMS antenna element in the x–y plane.
θ_T, θ_R	The antenna orientations of TMS and SBS, respectively.

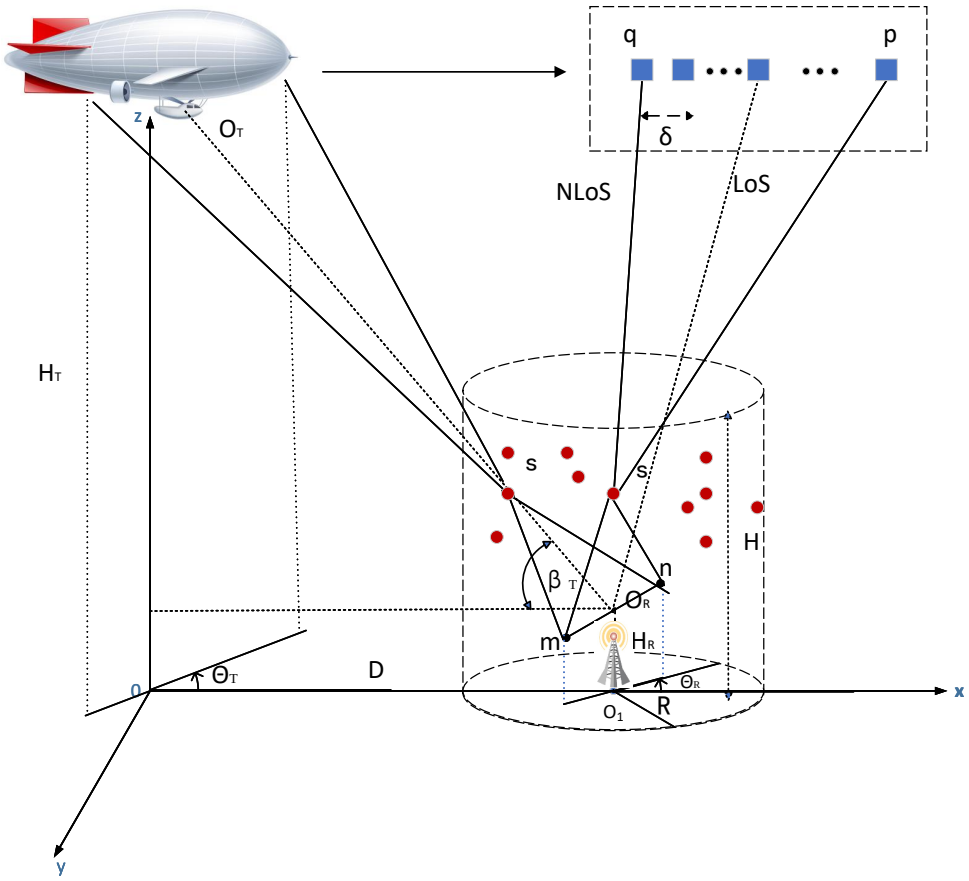

Figure 1. 3D GBSM with LoS and NLoS components for HAP-MIMO channel.

The general form of the S–T communication channel follows a Rice distribution, which effectively describes the statistical characteristics of the channel. Considering the geometric model depicted in Figure 1, it is evident that the channel impulse response is a result of the superposition of LoS components and NLoS components. i.e., [32]

$$h_{pn}(t;\tau) = h_{pn,\mathrm{LoS}}(t;\tau) + h_{pn,\mathrm{NLoS}}(t;\tau), \tag{2}$$

where

$$h_{pn,\mathrm{LoS}}(t;\tau) = \sqrt{\frac{K}{K+1}} e^{-j\frac{2\pi}{\lambda}d(p,n)} e^{j2\pi t f_{pn}^{\mathrm{LoS}}(t)} \delta(\tau - \tau_{\mathrm{LoS}}), \tag{3}$$

$$h_{pn,\mathrm{NLoS}}(t;\tau) = \sqrt{\frac{K}{K+1}} \frac{1}{\sqrt{N}} \sum_{i=1}^{N} e^{-j\frac{2\pi}{\lambda}(d(p,s)+d(s,n))+j\varphi(i)} e^{j2\pi t f_{pn}^{\mathrm{NLoS}}(t)} \delta(\tau - \tau_{\mathrm{NLoS}}^{(n)}), \tag{4}$$

where K and λ denote the Ricean factor and carrier wavelength, respectively; $d(p,n)$ denotes the distance between p and n; $f_{pn}^{\mathrm{LoS}}(t)$ and $f_{pn}^{\mathrm{NLoS}}(t)$ denote the Doppler frequency of the LoS components and NLoS components, respectively; $\varphi(n)$ denotes the phase introduced by the nth scatterer; τ_{LoS} and $\tau_{\mathrm{NLoS}}^{(n)}$ are the travel times of the LoS and NLoS waves, respectively; δ denotes the Dirac delta function. The Doppler frequency $f_{pn}^{\mathrm{LoS}}(t)$ and $f_{pn}^{\mathrm{NLoS}}(t)$ can be written as [32]

$$f_{pn}^{\mathrm{LoS}}(t) = f_{Tmax}cos(\pi - \alpha_{\mathrm{LoS}}(t) - \gamma_T) + f_{Rmax}cos(\alpha_{\mathrm{LoS}}(t) - \gamma_R), \tag{5}$$

$$f_{pn}^{\mathrm{NLoS}}(t) = f_{Tmax}cos(\gamma_T) + f_{Rmax}cos(\alpha_n(t) - \gamma_R)cos\beta_n(t), \tag{6}$$

where $f_{Tmax} = v_a/\lambda$ and $f_{Rmax} = v_b/\lambda$ denote the maximum Doppler frequencies associated with SBS and TMS, respectively. $\alpha_{\mathrm{LoS}}(t)$ denotes the azimuth angle of arrival (AAoA) of LoS components at the TMS. $\alpha_n(t)$ and $\beta_n(t)$ denote the azimuth angle of departure (AAoD) from the scatterer and the elevation angle of departure (EAoD) from the scatterer.

In the HAP channel, during the propagation of signals, electromagnetic waves are reflected, scattered, and diffracted due to factors such as buildings, trees, vegetation, terrain, and sea surface along the propagation path. This results in the signal reaching the receiving end being mixed with echoes propagated from multiple paths. The arrival time of each component of the multipath field at the receiving end is different, and multipath signals of different phases overlap with each other, causing interference to the signal and distorting the original signal. Errors may occur. Therefore, it is necessary to study the impact of this multipath effect on the channel and model the multipath effect accordingly.

The number of time-varying multipath is represented by $N(t)$. The time-varying number of multipath can be represented by a Poisson distribution for modeling the number of multipath. Its probability density function can be written as

$$P_{\mathrm{poisson}}(N(t)) = \frac{\rho^{N(t)}}{N(t)!}\mathrm{e}^{-\rho}, \tag{7}$$

where ρ denotes the mean of $N(t)$.

The delay of the k-th path is represented by the $\tau_{\mathrm{k}}(t)$, where the LoS path delay is between the HAP and the ground station. The NLoS path component delay can be obtained based on the increment of the LoS path delay, and its distribution is affected by the communication scenario and elevation angle. The delay increment of each multipath relative to the straight path is described using an exponential distribution, and its probability density function can be written as

$$P_{\exp}(\Delta\tau_k(t)) = \frac{1}{b}\mathrm{e}^{-\frac{\Delta\tau_k(t)}{b}}, \tag{8}$$

where b denotes the mean delay increment of each path.

The amplitude of the k-th path is represented by $a_k(t)$. Its probability density function can be expressed as

$$P(a_k(t)) = \frac{a_k(t)}{{\sigma_k}^2}\exp\left(-\frac{a_k(t)}{2{\sigma_k}^2}\right), \tag{9}$$

where $2{\sigma_k}^2(t)$ represents the average power of the Rayleigh distribution.

2.2. Birth–Death Process

The clusters in the HAP-MIMO channel represent groups of signal paths that result from reflections, diffractions, and scattering phenomena. These clusters exhibit dynamic characteristics due to the movement of the SBS and the changing positions of scatterers in the environment. The Markov birth–death process is a stochastic model that describes the evolution of a system where elements can either "birth" or "die" over time, with transition probabilities between different states.

To be able to talk about a Markov process, the three properties of stationarity, regularity, and independence, on which the derivation of the characteristics is based, should be

satisfied. Stability refers to the fact that the probability of a system's state transition remains constant over time. We assume that the statistical properties of the HAP channel are stable over a long time scale, meaning that the statistical properties of the channel do not change over time. Regularity requires that the state transition probability of the system is finite and non-zero. In HAP channel modeling, we assume that there is a non-zero probability of transitions between channel states, and these probabilities are finite. Independence refers to the fact that the future state of a system depends only on the current state and is independent of past states. In HAP channel modeling, we assume that the transition of channel states is independent of previous states, meaning that future channel states only depend on the current channel state.

In the context of HAP-MIMO channel modeling, the clusters are represented as states in the Markov process, and the birth and death events correspond to the creation or disappearance of clusters as the wireless environment changes [36]. The variability of the wireless channel over time primarily arises from the mobility of the TMS and the SBS. As these entities move, the wireless channel experiences change due to variations in path loss, shadowing, and interference conditions. Such dynamic characteristics contribute to the time-varying nature of the wireless channel in this context. Therefore, the time-varying channel fluctuations caused by the motion of the above two during the period from t to $t + \Delta t$ can be expressed as [19]

$$\delta_P(t, \Delta t) = \delta_{\mathrm{SBS}}(t, \Delta t) + \delta_{\mathrm{TMS}}(t, \Delta t), \tag{10}$$

where $\delta_{\mathrm{SBS}}(t, \Delta t)$ and $\delta_{\mathrm{TMS}}(t, \Delta t)$ represent time variation caused by SBS and TMS, respectively, and can be defined as

$$\delta_{\mathrm{SBS}}(t, \Delta t) = \int_t^{t+\Delta t} v_{\mathrm{SBS}}(t)dt, \tag{11}$$

$$\delta_{\mathrm{TMS}}(t, \Delta t) = \int_t^{t+\Delta t} v_{\mathrm{TMS}}(t)dt. \tag{12}$$

Due to the short time interval, we assume that SBS and TMS are in uniform motion. The above two equations can be simplified as [19]

$$\delta_{\mathrm{SBS}}(t, \Delta t) = v_{\mathrm{SBS}}(t) \times \Delta t, \tag{13}$$

$$\delta_{\mathrm{TMS}}(t, \Delta t) = v_{\mathrm{TMS}}(t) \times \Delta t. \tag{14}$$

Therefore, $\delta_P(t, \Delta t)$ gives the degree of correlation between CIR at different time instants. We introduce a Markov birth–death description that leads to the time-varying number $N(t)$ of clusters for CIR realizations. It can be divided at any time into newly generated and previously existing clusters. The Markov process can be described by the generation rate of clusters (λ_G) and the recombination rate of clusters (λ_R). The expectation of the total scatterer number is given by [19]

$$E\{N(t)\} = N(t_0) = \frac{\lambda_G}{\lambda_R}. \tag{15}$$

Each cluster survives from one CIR at t to the next one at $t + \Delta t$ with the following probability:

$$P_{sur}(\Delta t) = e^{-\lambda_R \frac{\delta_P(t,\Delta t)}{D_c}}, \tag{16}$$

where D_c is the related factor that changes with the scenario. The expected number of new clusters generated by Markov processes during the period $[t, t + \Delta t]$ is

$$E\{new(\Delta t)\} = \frac{\lambda_G}{\lambda_R}(1 - e^{-\lambda_R \frac{\delta_P(t,\Delta t)}{D_c}}). \tag{17}$$

We use scenario movement $\delta_P(t, \Delta t)$ to describe the correlation between two clusters. When the $\delta_P(t, \Delta t)$ value is high, the correlation between the properties of the existing clusters at t and the newly generated clusters at $t + \Delta t$ decreases. Figure 2 shows the image of the multipath components (MPCs) of the birth–death process, which assumes $\lambda_G = 0.13/\text{m}$ and $\lambda_R = 0.03/\text{m}$.

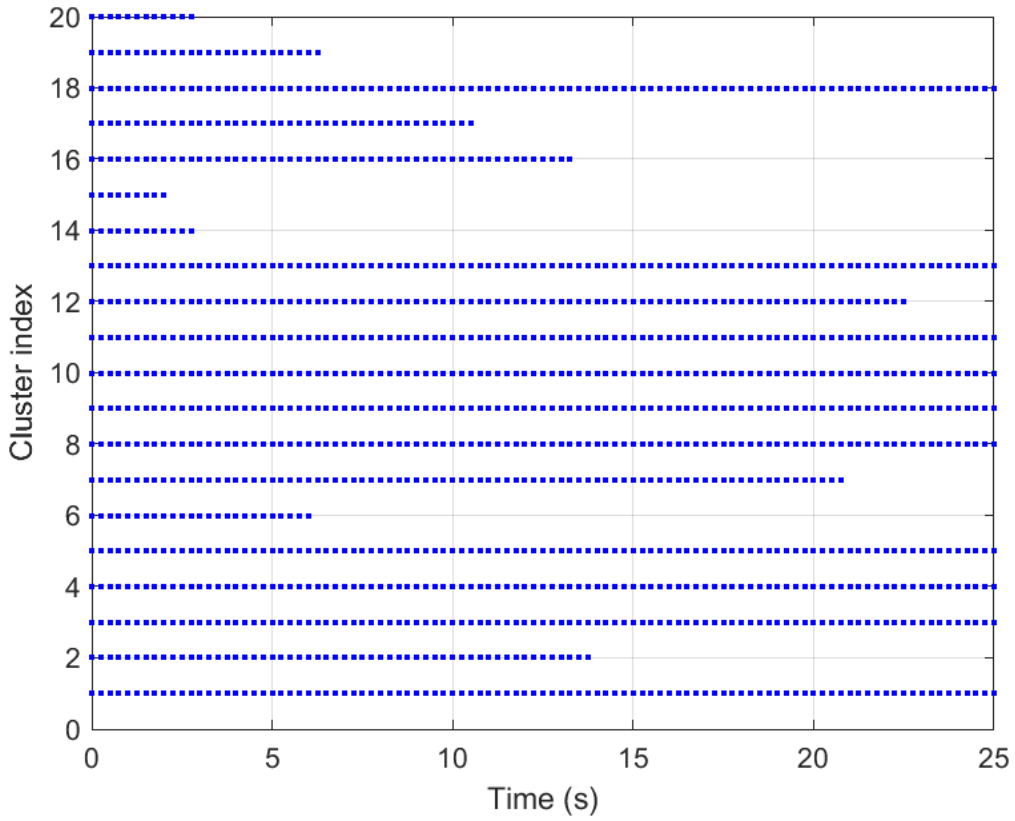

Figure 2. An example of the MPCs evolution process in the time domain ($\lambda_G = 0.13/\text{m}$, $\lambda_R = 0.03/\text{m}$).

Since both SBS and TMS are moving, the distance between clusters is time-varying, during the generation process of the new cluster, the time delay can be approximated as

$$\tau_l = \tau_{\text{LoS}(t)}, \tag{18}$$

where $\tau_{\text{LoS}(t)}$ represents the time-varying delay of the LoS path, and can be expressed as

$$\tau_{\text{LoS}(t)} = D_{\text{LoS}(t)}/c, \tag{19}$$

$$D_{\text{LoS}}(t) = d(p, n) + v_a \Delta t + v_b \Delta t. \tag{20}$$

Indeed, at the beginning, some scatterers are generated at the TMS end. Specific clusters may be removed from the CIR as time progresses, while new clusters may emerge. Additionally, the parameters associated with the surviving clusters changes within a time interval (Δt) due to the movement of SBS and TMS. To capture this dynamic evolution of the surviving clusters, it is necessary to incorporate an appropriate model that accounts for the changes in cluster parameters over time (Δt). This evolution process allows for adapting cluster characteristics in response to the movement and varying conditions in the wireless channel. By integrating these dynamics into the model, a more accurate representation of the CIR and their correlation over time can be achieved.

2.3. Large-Scale Parameters

HAP is located at the altitude of the stratosphere, and its propagation environment is very different from traditional ground communication or low altitude communication systems. The complex propagation environment requires large-scale parameters to characterize it. Due to the relatively long propagation distance between HAP and ground terminals, path loss increases with distance, and free space loss is the most basic part, which can help us accurately evaluate signal attenuation. The weather conditions in the stratosphere can also have a significant impact on signal propagation, and our HAP channel is located in the mmWave band with a high frequency, so rainfall attenuation is also an important factor that we need to consider. Therefore, it is important to consider large-scale parameters, such as free space loss and rainfall attenuation, in HAP channel modeling.

When wireless signals propagate through the atmosphere, they encounter various atmospheric components that affect their transmission. The primary atmospheric components contributing to this attenuation are dry air molecules and water molecules in the atmosphere. To calculate the attenuation caused by atmospheric absorption on transmission signals, we can refer to the ITU-R P.676 [37], which provides an atmospheric molecular absorption attenuation prediction model. The oblique path gas attenuation can be estimated by dividing the atmosphere into exponentially increasing layers, determining the specific attenuation (dB/km) of each layer and the path length (km) passing through each layer. The product of the specific attenuation of each layer and the path length passing through each layer can be summed up to provide a very approximate estimation. The molecular absorption loss is represented by [37]

$$A_{gas} = \sum_{i=1}^{i_{\max}} \omega_i H_i, \tag{21}$$

where H_i denotes the distance of the path and ω_i denotes the ratio decline, which relates to dry air pressure, water vapor partial pressure, and ambient temperature. We use the simulation data of the global annual average reference atmosphere in the ITU-R P.835 [38].

The rainfall process introduces a significant complexity to the attenuation of the HAP channel. To compute the attenuation caused by rainfall on transmission signals in the HAP channel, we can refer to the rainfall attenuation prediction model provided in the ITU-R P.618 [39]. This prediction model incorporates factors such as the actual propagation distance, rainfall rate, and height of the rainfall in the HAP channel. This model can replace the path loss caused by rainfall in the HAP communication environment with an equivalent tilted path and unit kilometer attenuation. The rainfall attenuation can be expressed as [39]

$$A_{rain} = \gamma_R \times L_E, \tag{22}$$

which can be derived from the ITU-R P.618 recommendation. Where γ_R denotes unit kilometer ratio fading. It is related to rainfall rate and communication frequency. L_E denotes effective inclined path length. The length of the tilted path is related to the communication elevation and orbit height and requires frequency correlation coefficient correction to obtain an effective tilted path length.

3. GBSM Non-Stationary Channel Statistical Properties

In this section, we present the distribution of scatterers and derive formulas for temporal ACF, spatial CCF, and FCF. The cylinder model based on GBSM is shown in Figure 3, we use different distributions to describe the azimuth and elevation angles of scatterers, respectively. We assume that the azimuth angles φ_z and elevation angles θ_z of the received signal are independent, φ_z follows von-Mises distribution, and θ_z follows Laplacian distribution [31,40]. Specifically, the von-Mises distribution can simulate some typical channel characteristics well, such as multipath scattering in the HAP channel. Moreover, the parameters of the von-Mises distribution can reflect the correlation and spatial coherence characteristics of the channel, which more comprehensively describes the

channel state transition process. Similarly, the Laplacian distribution has similar advantages in describing elevation angle distributions. It can well describe phenomena such as high correlation and vertical signal attenuation in the HAP channel. The scatterers distribution map can be outlined as follows

$$f_1(\varphi_z) = \frac{exp(k_1(\varphi_z - \overline{\varphi_z}))}{2\pi I_0(k_1)}, -\pi \le \varphi_z, \overline{\varphi_z} \le \pi, \tag{23}$$

$$f_2(\theta_z) = \frac{\pi}{4\theta_m} cos(\frac{\pi(\theta_z - \overline{\theta_z})}{2\theta_z}), \overline{\theta_z} - \theta_m \le \theta_z \le \overline{\theta_z} + \theta_m \le \pi/2, \tag{24}$$

where $I_0(.)$ is the zero-order Bessel function and k_1 controls the density of $f_1(\varphi_z)$, setting $k_1 = 0$ incurs isotropic scattering, i.e., $f_1(\varphi_z) = 1/2\pi$. As k_1 increases, the scattering becomes increasingly non-isotropic. $\overline{\varphi_z}$, and $\overline{\theta_z}$ are the mean values of φ_z and θ_z, respectively, and θ_m denotes the maximum elevation angle in the communication environment.

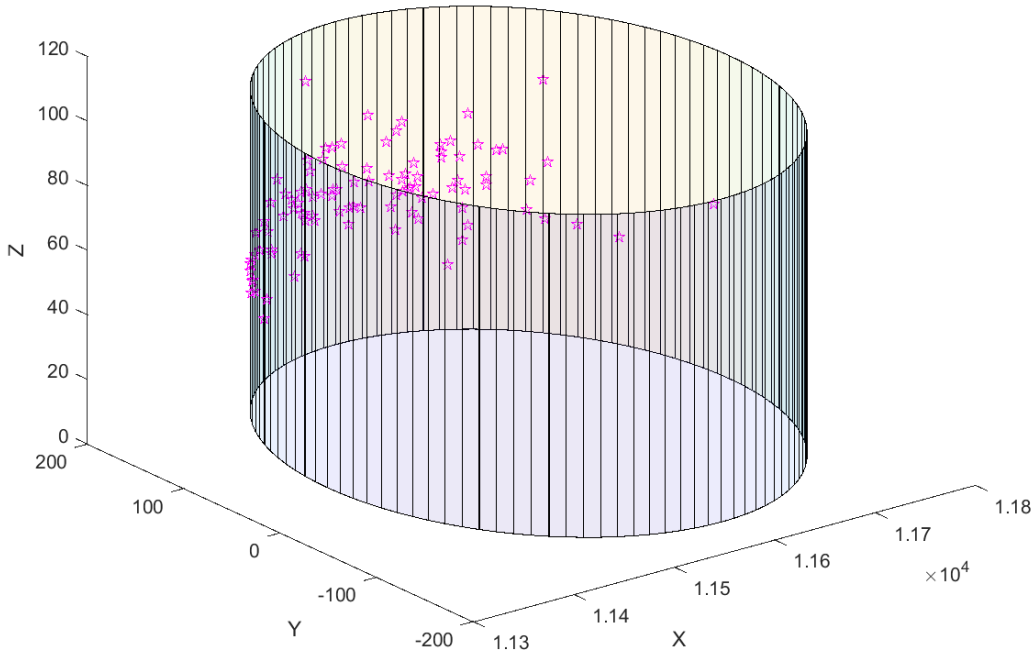

Figure 3. Scatterers in the cylinder distribution-map.

The non-stationary nature of the channel can be reflected through the correlation function. This chapter models the channel model for non-stationary characteristics in the time, space, and frequency domains. By calculating and comparing the consistency of the changes in the two parameters of the correlation function, the non-stationary nature of the channel with the changes in the above parameters can be verified separately [41].

$$\begin{aligned} &R_{qm,pn}(t, f; \Delta r, \Delta t, \Delta f) = E[h^*_{qm,pn}(t, f) h_{\Delta r}(t + \Delta t, f + \Delta f)] \\ &= \tfrac{K}{K+1} R^{\text{LoS}}_{qm,pn}(t, f, \Delta r, \Delta t, \Delta f) + \tfrac{1}{K+1} \sum_{\text{m=1}}^{M} R^{\text{NLoS}}_{qm,pn}(t, f, \Delta r, \Delta t, \Delta f) \end{aligned}, \tag{25}$$

where (.)* denotes complex conjugate operation, E [.] denotes the statistical expectation operation.

3.1. Temporal ACF

Considering the birth–death process, the survival probability of a cluster in the range of t to $t + \Delta t$ is $e^{-\lambda_R P_c(v_a \Delta t + v_b \Delta t)}$. The proposed GBSM normalized ACF between $q - m$ link and $p - n$ link can be defined as [41]

$$R_{qm,pn}(t, \Delta t) = R^{\text{LoS}}_{qm,pn}(t, \Delta t) + R^{\text{NLoS}}_{qm,pn}(t, \Delta t), \tag{26}$$

$$R_{qm,pn}^{\mathrm{LoS}}(t,\Delta t) = e^{-\lambda_R P_c(v_a\Delta t+v_b\Delta t)} \times \frac{K}{K+1} e^{-j2\pi(d(p,l)(t)-d(q,m)(t+\Delta t))} \times e^{-j2\pi\Delta t(f_{Tmax}cos(\gamma_T)+f_{Rmax}cos(\pi-\gamma_R))}, \quad (27)$$

$$R_{qm,pn}^{\mathrm{NLoS}}(t,\Delta t) = e^{-\lambda_R(v_{TMS}\Delta t+v_{SBS}\Delta t)} \times \frac{1}{K+1}\int_{R_{\min}}^{R_{\max}}\int_{\beta_{\min}}^{\beta_{\max}} f_1(\varphi_z)\times f_2(\theta_z) \times e^{-\frac{2\pi}{\lambda}(d(p,s)(t)+d(s,n)(t)-d(q,s)(t-\Delta t)-d(s,m)(t-\Delta t))} \times e^{-\frac{2\pi}{\lambda}(v_a+v_b)\Delta t\cos(\alpha_n(t)-\gamma_R)\cos(\beta_n(t))} d\alpha d\beta, \quad (28)$$

where $R_{\min}$ and $R_{\max}$ denote the minimum and maximum horizontal distance between the scatterer s and O_R, and the symbols $\beta_{\min}$ and $\beta_{\max}$ denote the minimum and maximum EAoD, respectively.

3.2. Spatial CCF

In wide-sense stationary uncorrelated scattering (WSSUS) channels, the spatial CCF depends on the relative SBS and TMS antenna element spacing δ_T and δ_R, respectively. However, for non-stationary systems, spatial CCF is not only related to relative antenna spacing but also to time t. Therefore, based on this dependency, the spatial CCF of the non-stationary channel model can be referred to as the local spatial CCF and can be expressed as [41]

$$R_{qm,pn;\Delta q,\Delta p}(t,f) = R_{qm,pn;\Delta q,\Delta p}^{\mathrm{LoS}}(t,f) + R_{qm,pn;\Delta q,\Delta p}^{\mathrm{NLoS}}(t,f), \quad (29)$$

$$R_{qm,pn;\Delta q,\Delta p}^{\mathrm{LoS}}(t,f) = \frac{K}{K+1}E[\mathrm{h}_{qm,pn}^{\mathrm{LoS}^*}(t)h_{qm,pn;\Delta q,\Delta p}^{\mathrm{LoS}}(t)e^{j2\pi\Omega_{f,1}}], \quad (30)$$

$$R_{qm,pn;\Delta q,\Delta p}^{\mathrm{NLoS}}(t,f) = \frac{K}{K+1}\sum_{i=1}^{n}E[\mathrm{h}_{qm,pn}^{i^*}(t)h_{qm,pn;\Delta q,\Delta p}^{i}(t)e^{j2\pi\Omega_{f,2}}], \quad (31)$$

$$\Omega_{f,1} = f(\tau_{qm,pn}^{\mathrm{LoS}}(t)-\tau_{qm,pn}^{\mathrm{LoS}}(t+\Delta t)), \Omega_{f,2} = f(\tau_{qm,pn}^{i}(t)-\tau_{qm,pn}^{i}(t+\Delta t)), \quad (32)$$

where n denotes the number of scatterers and τ denotes the delay of each path.

3.3. FCF

We mainly consider the HAP channel in the mmWave bands, where signals are subjected to stronger attenuation and multipath effects, leading to frequency fading and other phenomena during signal propagation. Therefore, we need to discuss the correlation function and non-stationary characteristics of HAP channels. By setting the time increment Δt and the antenna space increment Δq, Δp to zero, FCF can be expressed as [41]

$$R_{qm,pn}(t,f;\Delta f) = R_{qm,pn}^{\mathrm{LoS}}(t,f;\Delta f) + R_{qm,pn}^{\mathrm{NLoS}}(t,f;\Delta f), \quad (33)$$

$$R_{qm,pn}^{\mathrm{LoS}}(t,f;\Delta f) = \frac{K}{K+1}E[\mathrm{h}_{qm,pn}^{\mathrm{LoS}^*}(f)(\frac{f}{f_c})^{\mathrm{LoS}^*}h_{qm,pn}^{\mathrm{LoS}}(f+\Delta f)(\frac{f+\Delta f}{f_c})^{\mathrm{LoS}}e^{j2\pi\Omega_{f,1}}], \quad (34)$$

$$R_{qm,pn}^{\mathrm{NLoS}}(t,f;\Delta f) = \frac{1}{K+1}\sum_{\mathrm{i}=1}^{\mathrm{n}}E[\mathrm{h}_{qm,pn}^{i}(f)(\frac{f}{f_c})^{\gamma_i^*}h_{qm,pn}^{i}(f+\Delta f)(\frac{f+\Delta f}{f_c})^{\gamma_i}e^{j2\pi\Omega_{f,2}}]. \quad (35)$$

4. Results and Analysis

In our simulation process, we consider HAP-MIMO communication scenarios. Unless otherwise specified, the following parameters are selected: f = 38 GHz, n_T = 64, n_R = 2, β_T = 60°, $\theta_T = \theta_R$ = 45°, ψ_R = 0°, H_T = 20 km, H_R = 10 m, k = 4, μ = 0°, H = 100 m, R = 200 m; we refer to a typical densely built area in London and set the average height of scatterers as H_{mean} = 17.6 m and σ = 0.31, K = 3 dB, v_a = 50 m/s, v_b = 5 m/s, λ_G = 0.13/m, λ_R = 0.03/m, n = 40. Figure 4 shows that the attenuation increases with increasing rainfall intensity in the HAP channel.

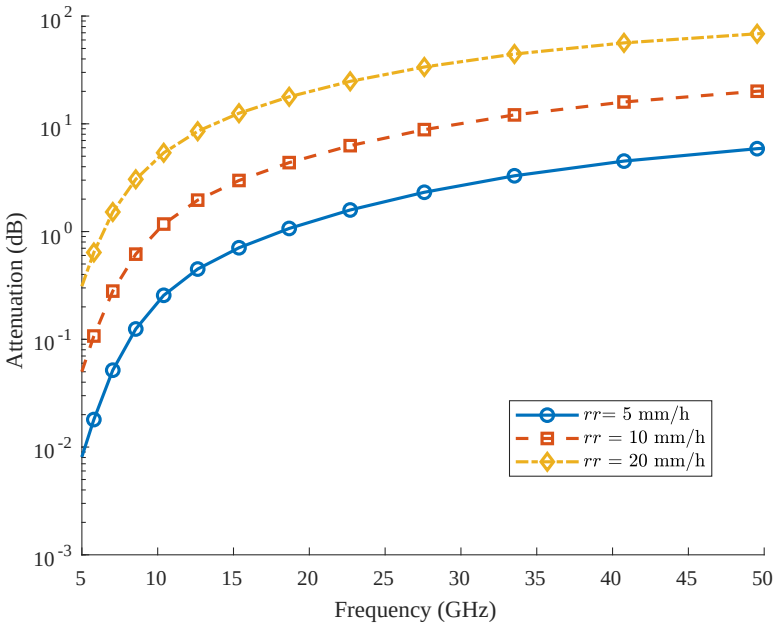

Figure 4. Path loss for different rain-rates.

In Table 2, we compare our model with Model in [31] and Model in [32].

Table 2. Comparison among our model and Model in [31] and Model in [32].

Our Model	**Model in [31]**	**Model in [32]**
GBSM	GBSM	GBSM
Consider birth–death process	Consider birth–death process	Not consider birth–death process
Consider large-scale parameters	Not consider large-scale parameters	Not consider large-scale parameters
Consider temporal ACF	Consider temporal ACF	Consider temporal ACF
Consider spatial CCF	Consider spatial CCF	Not consider spatial CCF
Consider FCF	Not consider FCF	Not consider FCF

From the table, it can be seen that our manuscript considers non-stationary characteristics from time domain, space domain, and frequency domain, and also takes into account the influence of large-scale parameters on channel attenuation. By considering these factors, our model can more accurately describe the characteristics of actual channels.

Due to the mutual movement between SBS and TMS, the channel model exhibits non-stationary characteristics in the time domain. Figure 5 shows the variation of time-domain normalized ACF with time interval Δt at three different starting times t = 0 s, t = 2 s, and t = 4 s. As shown in the figure, the temporal ACF for different simulation starting times has significant differences. The theoretical results and simulation results are basically consistent. Therefore, the proposed model can characterize the non-stationary characteristics in the time domain.

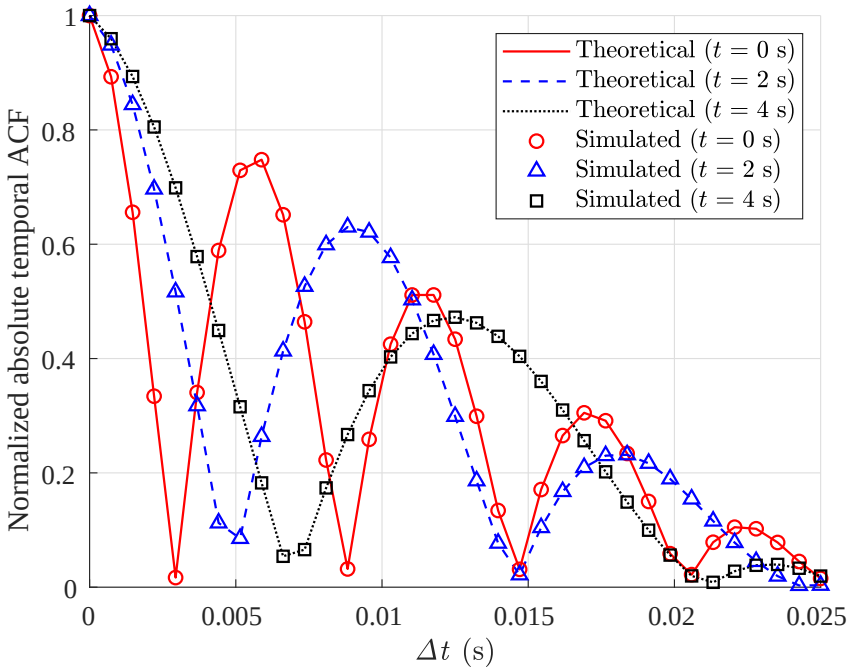

Figure 5. Temporal ACF results at different times.

Figure 6 depicts the variation of the temporal ACF with different elevation angles β_T at t = 0 s; as shown in the figure, the increase in β_T leads to a sharp decrease in temporal correlation. In the HAP system, when the elevation angle changes, the length and propagation time of the signal propagation path also change accordingly. This results in different multipath signals reaching the TMS at different phases, thereby affecting the temporal ACF of the signal. As the elevation angle increases, the signal propagation environment changes more dramatically, the diversity of signal propagation paths increases, and multipath effects become more significant. Therefore, the impact of HAP motion on time correlation is decreasing.

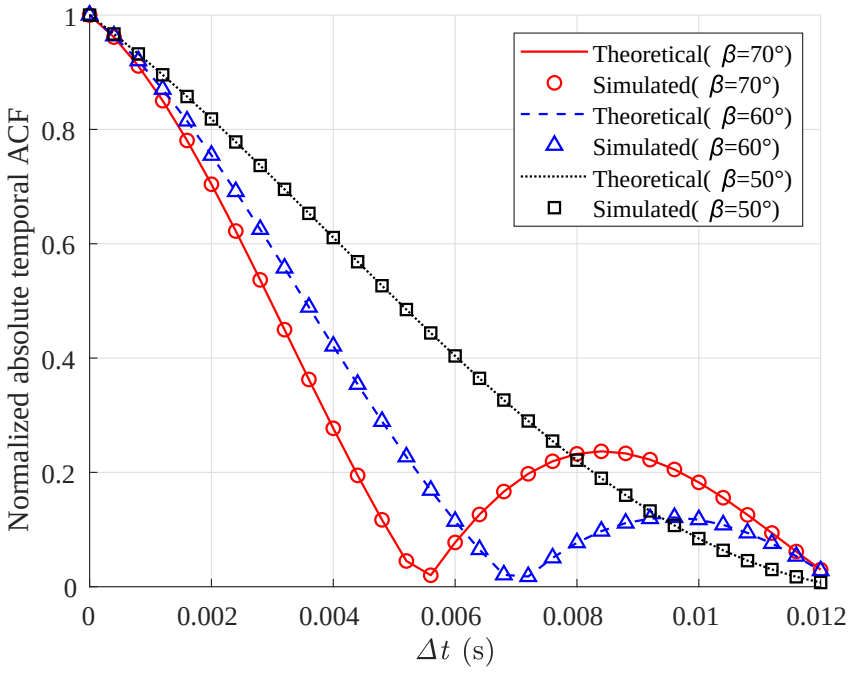

Figure 6. Temporal ACF results at different elevation angles (t = 0 s).

Figure 7 shows the temporal ACF between the isotropic environment $k = 0$ and the non-isotropic environment $k = 4$ and $k = 10$. It can be seen that, as k increases, the distribution of scatterers becomes more concentrated and the correlation becomes higher.

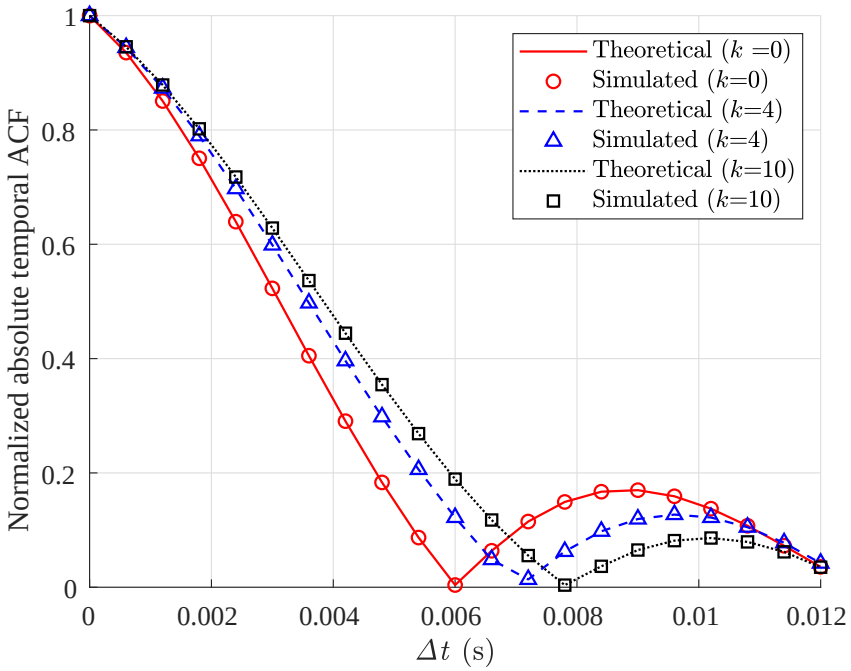

Figure 7. Temporal ACF results at different degrees of scatterer aggregation (t = 0 s).

Due to the drastic changes in the channel caused by the near-field effect with the antenna array, the massive MIMO channel we use exhibits non-stationary characteristics in the space domain. We calculate the changes in the space domain normalized cross-correlation function with the array element spacing Δp for three sets of transmitting and receiving antenna pairs $p = 1$, $q = 1$, $p = 32$, $q = 1$, and $p = 64$, $q = 2$, respectively. Figure 8 shows that the spatial CCF of different receiving and transmitting antenna pairs is significantly different. This is because different antennas have different positions and directions in space. Due to the different positions and directions of different antennas, the propagation paths experienced by the signals they receive will also vary. This results in signals between different antennas having different delays and phase differences, leading to changes in spatial CCF. The theoretical and simulation results are in good agreement. Therefore, the proposed channel model can describe the non-stationary nature of channels in the space domain.

Due to the non-uniform fading characteristics of wideband at different frequency points, the GBSM channel model of HAP exhibits non-stationary characteristics in the frequency domain. In Figure 9, it can be seen that the normalized CCF in the frequency domain varies with the frequency interval Δf at three different starting frequencies $f = 38$ GHz, $f = 38.5$ GHz, and $f = 39$ GHz. From the figure, it can be seen that the CCF at different simulation frequencies has a significant difference. Our HAP channel is located in mmWave and has a large bandwidth, wideband HAP channel has different fading characteristics at different frequency. Therefore, it exhibits non-stationary characteristics in the frequency domain. The theoretical results and simulation results are basically consistent. Therefore, the proposed channel model can describe the non-stationary nature of channels in the frequency domain.

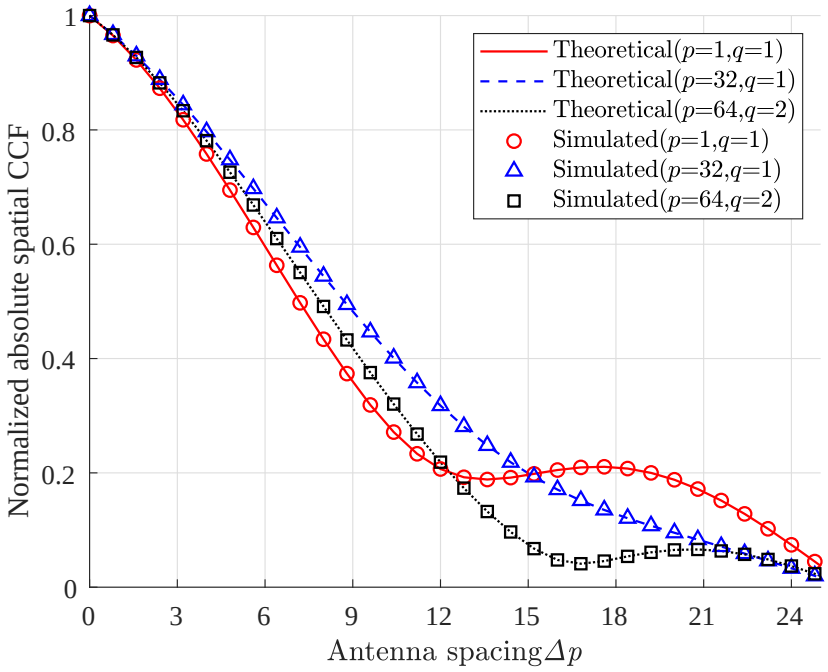

Figure 8. Spatial CCF under different antenna spacing.

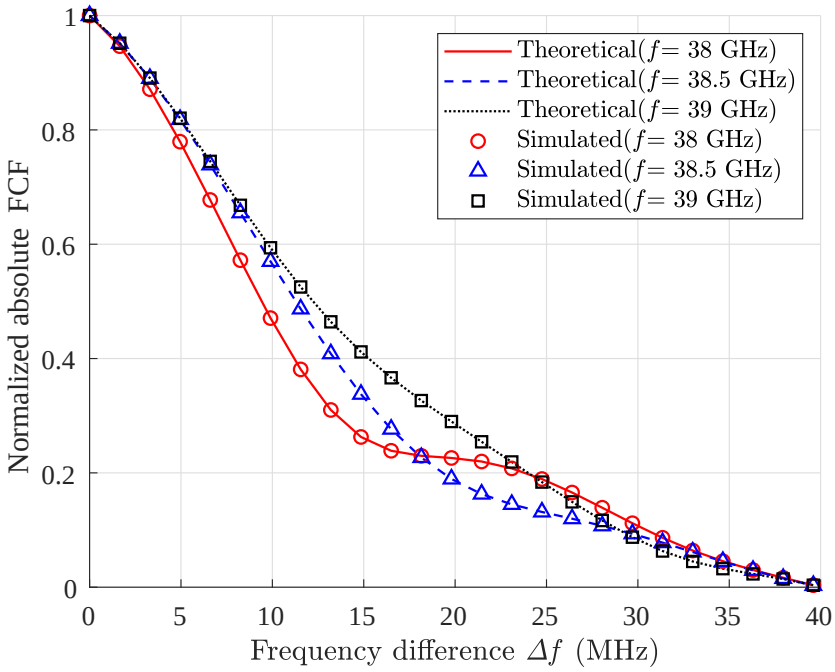

Figure 9. CCF under different frequencies.

The cumulative distribution functions (CDF) of the stationary bandwidth of our channel model at different frequencies and the model in [31] and the model in [32] are shown in Figure 10. The threshold is chosen as 0.9. The model in [31] and the model in [32] did not consider FCF, and the stationary bandwidth is infinite. The channel whose bandwidth less than the stationary interval can be considered as frequency stationary. Therefore, in the case of wide bandwidth at the mmWave band, it is necessary to consider the non-stationary characteristics of the frequency.

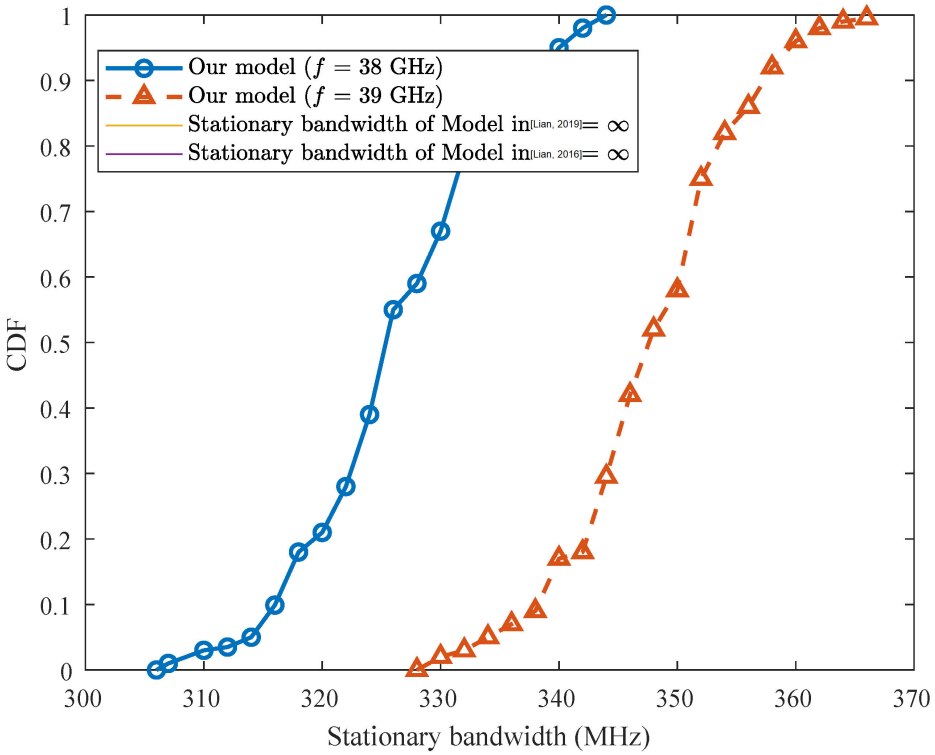

Figure 10. Comparison of stationary bandwidth [31,32].

5. Conclusions

In this paper, we investigated a non-stationary 3D GBSM for HAP-MIMO communication systems at mmWave bands. We utilized a cylinder-based geometric modeling method to construct the channel and derived the channel impulse response. The Markov process was used to describe scatterers' birth–death process. The impact of large-scale parameters, such as free space loss and rainfall loss was considered in our proposed model. Furthermore, we derived the temporal ACF and obtained the effects of parameters such as elevation angles and scatterer distribution on the correlation of the model. Additionally, we obtained the spatial CCF and FCF and conducted simulation. Theoretical results were consistent with the simulation results, which showed that the constructed 3D GBSM model could effectively characterize the non-stationary characteristics of HAP-MIMO channels in the time, space, and frequency domains.

The significance of this work lies in the fact that it provides a comprehensive and accurate model for HAP-MIMO communication systems at mmWave bands. The non-stationary 3D GBSM takes into account the large-scale parameters and can effectively describe the non-stationary characteristics in time, space, and frequency domains. This model can be used to optimize the design of HAP-MIMO systems and improve their performance. Our work can help fill the gap in existing literature on the non-stationary characteristics of frequencies at the mmWave band, and supplement some research on path loss. In future work, we plan to continue improving our non-stationary 3D GBSM by introducing more large-scale parameters and using machine learning methods to adjust the parameters to improve the accuracy of the model.

Author Contributions: Conceptualization, L.G. and W.Z.; methodology, L.G.; software, L.G. and K.Z.; validation, L.G. and K.Z.; formal analysis, L.G. and Z.J.; investigation, L.G.; resources, L.G.; data curation, L.G. and S.W.; writing—original draft preparation, L.G.; writing—review and editing, Y.Z.; visualization, L.G.; supervision, W.Z. and Y.Z.; project administration, W.Z.; funding acquisition, Y.Z. All authors have read and agreed to the published version of the manuscript.

Funding: This work was supported by the National Natural Science Foundation of China under Grant 62271051 and Grant 61871035, and Defense Industrial Technology Development Program, China under Grant JCKY2022209A001.

Data Availability Statement: Data is contained within the article. The data presented in this study are available in Section 4.

Conflicts of Interest: The authors declare no conflicts of interest.

References

1. Nguyen, D.C.; Ding, M.; Pathirana, P.N.; Seneviratne, A.; Li, J.; Niyato, D.; Dobre, O.; Poor, H.V. 6G Internet of Things: A Comprehensive Survey. *IEEE Internet Things J.* **2022**, *9*, 359–383. [CrossRef]
2. Wang, C.X.; You, X.; Gao, X.; Zhu, X.; Li, Z.; Zhang, C.; Wang, H.; Huang, Y.; Chen, Y.; Haas, H.; et al. On the Road to 6G: Visions, Requirements, Key Technologies, and Testbeds. *IEEE Commun. Surv. Tutor.* **2023**, *25*, 905–974. [CrossRef]
3. Cao, K.; Ding, H.; Li, W.; Lv, L.; Gao, M.; Gong, F.; Wang, B. On the Ergodic Secrecy Capacity of Intelligent Reflecting Surface Aided Wireless Powered Communication Systems. *IEEE Wirel. Commun. Lett.* **2022**, *11*, 2275–2279. [CrossRef]
4. Kırık, M.; Abusanad, N.A.; Arslan, H. Inter-HAP Based Geometrical 3D Channel Model Operating at 28 to 60 GHz for Future 6G Non-Terrestrial Networks. In Proceedings of the 2023 IEEE Wireless Communications and Networking Conference (WCNC), Glasgow, UK, 26–29 March 2023; Volume 16, p. 168.
5. Zheng, W.; Gong, G.; Tian, J.; Lu, S.; Wang, R.; Yin, Z.; Li, X.; Yin, L. Design of a Modified Transformer Architecture Based on Relative Position Coding. *Int. J. Comput. Intell. Syst.* **2023**, *16*, 168. [CrossRef]
6. Chen, S.; Sun, S.; Kang, S. System integration of terrestrial mobile communication and satellite communication—The trends, challenges and key technologies in B5G and 6G. *China Commun.* **2020**, *17*, 156–171. [CrossRef]
7. Hassan, M.S.; Saha, C.; Lianghai, J.; Alvarino, A.R.; Ma, J.; Liu, L.; Wu, Q. *NTN: From 5G NR to 6G*; IEEE: Piscataway, NJ, USA, 2023; pp. 173–178.
8. Omote, H.; Kimura, S.; Lin, H.Y.; Sato, A. HAPS propagation loss model for urban and suburban environments. In Proceedings of the 2020 International Symposium on Antennas and Propagation (ISAP), Osaka, Japan, 25–28 January 2021; pp. 681–682.
9. Ma, K.; Li, Z.; Liu, P.; Yang, J.; Geng, Y.; Yang, B.; Guan, X. Reliability-Constrained Throughput Optimization of Industrial Wireless Sensor Networks With Energy Harvesting Relay. *IEEE Internet Things J.* **2021**, *8*, 13343–13354. [CrossRef]
10. Palanci, C.; Akleman, F.; Kurt, G.K. High Altitude Platform Station (HAPS) to Satellite Channel Models for 6G Networks. In Proceedings of the 2022 IEEE Aerospace Conference (AERO), Big Sky, MT, USA, 5–12 March 2022; pp. 1–10.
11. Feasibility Study of High Altitude Platform Station (HAPS) Implementation for Urban Areas in Indonesia: A Case Study of East Kalimantan. In Proceedings of the 2023 IEEE International Opportunity Research Scholars Symposium (ORSS), Atlanta, GA, USA, 23 April–2 June 2023; pp. 92–95.
12. Lian, Z.; Jiang, L.; He, C.; He, D. User Grouping and Beamforming for HAP Massive MIMO Systems Based on Statistical-Eigenmode. *IEEE Wirel. Commun. Lett.* **2019**, *8*, 961–964. [CrossRef]
13. Xu, J.; Cheng, X.; Bai, L. A 3D Space-Time-Frequency Non-Stationary Model for Low-Altitude UAV mmWave and Massive MIMO Aerial Fading Channels. *IEEE Trans. Antennas Propag.* **2022**, *70*, 10936–10950. [CrossRef]
14. Wang, Q.; Li, P.; Rocca, P.; Li, R.; Tan, G.; Hu, N.; Xu, W. Interval-Based Tolerance Analysis Method for Petal Reflector Antenna With Random Surface and Deployment Errors. *IEEE Trans. Antennas Propag.* **2023**, *71*, 8556–8569. [CrossRef]
15. Jiang, Y.; Li, X. Broadband cancellation method in an adaptive co-site interference cancellation system. *Int. J. Electron.* **2022**, *109*, 854–874. [CrossRef]
16. Yang, W.; Xie, D.; Jing, X.; Jiang, Q.; Zeng, J. High Altitude Platform Station Communication as an Enabler for Massive Internet of Things. In Proceedings of the 2020 IEEE 20th International Conference on Communication Technology (ICCT), Nanning, China, 28–31 October 2020; pp. 829–833.
17. Ghazal, A.; Yuan, Y.; Wang, C.X.; Zhang, Y.; Yao, Q.; Zhou, H.; Duan, W. A Non-Stationary IMT-Advanced MIMO Channel Model for High-Mobility Wireless Communication Systems. *IEEE Trans. Wirel. Commun.* **2017**, *16*, 2057–2068. [CrossRef]
18. Lian, Z.; Jiang, L.; He, C.; Xi, Q. A Novel Channel Model for 3D HAP-MIMO Communication Systems. In Proceedings of the 2016 International Conference on Networking and Network Applications (NaNA), Hakodate, Japan, 23–25 July 2016; pp. 1–6.
19. Hu, J.; Jiang, L.; He, C.; Lian, Z.; Liu, J. A 3D HAP-MIMO channel model based on dynamic properties of scatterers. In Proceedings of the 2017 9th International Conference on Wireless Communications and Signal Processing (WCSP), Nanjing, China, 11–13 October 2017; pp. 1–5.
20. Lian, Z.; Jiang, L.; He, C. A 3D GBSM Based on Isotropic and Non-Isotropic Scattering for HAP-MIMO Channel. *IEEE Commun. Lett.* **2018**, *22*, 1090–1093. [CrossRef]
21. Michailidis, E.T.; Nomikos, N.; Trakadas, P.; Kanatas, A.G. Three-Dimensional Modeling of mmWave Doubly Massive MIMO Aerial Fading Channels. *IEEE Trans. Veh. Technol.* **2020**, *69*, 1190–1202. [CrossRef]
22. Zakia, I. Capacity of HAP-MIMO channels for high-speed train communications. In Proceedings of the 2017 3rd International Conference on Wireless and Telematics (ICWT), Palembang, Indonesia, 27–28 July 2017; pp. 26–30.

23. Zou, S.; Jiang, L.; Ji, P.; He, C.; He, D.; Zhang, G. Beam Selection Algorithm for Beamspace HAP-MIMO Systems Based on Statistical CSI. In Proceedings of the 2021 International Conference on Networking and Network Applications (NaNA), Lijiang City, China, 29 October–1 November 2021; pp. 47–51.
24. Yang, M.; Zhang, S.; Shao, X.; Guo, Q.; Tang, W. Statistical modeling of the high altitude platform dual-polarized MIMO propagation channel. *China Commun.* **2017**, *14*, 43–54. [CrossRef]
25. Lian, Z.; Su, Y.; Wang, Y.; Jiang, L. A Non-Stationary 3D Wideband Channel Model for Intelligent Reflecting Surface-Assisted HAP-MIMO Communication Systems. *IEEE Trans. Veh. Technol.* **2022**, *71*, 1109–1123. [CrossRef]
26. Toyoshima, M. Space Laser Communications for Beyond 5G/6G. In Proceedings of the 2023 Opto-Electronics and Communications Conference (OECC), Shanghai, China, 2–6 July 2023; pp. 1–2.
27. Aliouane, M.A.; Conrat, J.M.; Cousin, J.C.; Begaud, X. Material Reflection Measurements in Centimeter and Millimeter Wave ranges for 6G Wireless Communications. In Proceedings of the 2022 Joint European Conference on Networks and Communications & 6G Summit (EuCNC/6G Summit), Grenoble, France, 7–10 June 2022; pp. 43–48.
28. GSM Association. *An Introduction to the WRC: A Beginners Guide to the World Radiocommunication Conference*; GSM Association: Lodon, UK, 2017.
29. Zhao, J.; Wang, Q.; Li, Y.; Zhou, J.; Zhou, W. Ka-band Based Channel Modeling and Analysis in High Altitude Platform (HAP) System. In Proceedings of the 2020 IEEE 91st Vehicular Technology Conference (VTC2020-Spring), Antwerp, Belgium, 25–28 May 2020; pp. 1–5.
30. Lian, Z.; Jiang, L.; He, C. A 3D Wideband Model Based on Dynamic Evolution of Scatterers for HAP-MIMO Channel. *IEEE Commun. Lett.* **2017**, *21*, 684–687. [CrossRef]
31. Lian, Z.; Jiang, L.; He, C.; He, D. A Non-Stationary 3D Wideband GBSM for HAP-MIMO Communication Systems. *IEEE Trans. Veh. Technol.* **2019**, *68*, 1128–1139. [CrossRef]
32. Lian, Z.; Jiang, L.; He, C. A Non-stationary 3D Multi-cylinder Model for HAP-MIMO Communication Systems. In *Space Information Networks, Proceedings of the First International Conference, SINC 2016, Kunming, China, 24–25 August 2016*; Springer: Singapore, 2016; pp. 202–214.
33. Bai, L.; Wang, C.X.; Wu, S.; Wang, H.; Yang, Y. A 3D wideband multi-confocal ellipsoid model for wireless MIMO communication channels. In Proceedings of the 2016 IEEE International Conference on Communications (ICC), Kuala Lumpur, Malaysia, 22–27 May 2016; pp. 1–6.
34. Bai, L.; Wang, C.X.; Goussetis, G.; Wu, S.; Zhu, Q.; Zhou, W.; Aggoune, E.H.M. Channel Modeling for Satellite Communication Channels at Q-Band in High Latitude. *IEEE Access* **2019**, *7*, 137691–137703. [CrossRef]
35. Lian, Z.; Su, Y.; Wang, Y.; Jiang, L.; Zhang, Z.; Xie, Z.; Li, S. A Nonstationary 3D Wideband Channel Model for Low-Altitude UAV-MIMO Communication Systems. *IEEE Internet Things J.* **2022**, *9*, 5290–5303. [CrossRef]
36. Lian, Z.; Jiang, L.; He, C.; Xi, Q. A novel multiuser HAP-MIMO channel model based on birth–death process. In Proceedings of the 2016 IEEE International Conference on Communications (ICC), Kuala Lumpur, Malaysia, 22–27 May 2016; pp. 1–5.
37. *ITU-R P.676-11[R]*; Attenuation by Atmospheric Gases. ITU: Geneva, Switzerland, 2019.
38. *ITU-R P.835-6[R]*; Reference Standard Atmospheres. ITU: Geneva, Switzerland, 2017.
39. *ITU-R P.618-13[R]*; Propagation Data and Prediction Methods Required for the Design of Earth-Space Telecommunication Systems. ITU: Geneva, Switzerland, 2017.
40. Zhu, Q.; Yang, Y.; Chen, X.; Tan, Y.; Fu, Y.; Wang, C.X.; Li, W. A Novel 3D Non-Stationary Vehicle-to-Vehicle Channel Model and its Spatial-Temporal Correlation Properties. *IEEE Access* **2018**, *6*, 43633–43643. [CrossRef]
41. Bian, J.; Wang, C.X.; Gao, X.; You, X.; Zhang, M. A General 3D Non-Stationary Wireless Channel Model for 5G and Beyond. *IEEE Trans. Wirel. Commun.* **2021**, *20*, 3211–3224. [CrossRef]